Nanoscale Advances

ROYAL SOCIETY OF CHEMISTRY

PAPER

View Article Online
View Journal | View Issue

Cite this: *Nanoscale Adv.*, 2022, **4**, 916

A binder jet 3D printed MXene composite for strain sensing and energy storage application†

Terek Li, Tianhao Chen, Xuechen Shen, HaoTian Harvey Shi, Elahe Jabari and Hani E. Naguib *

Polymer composite materials have been proven to have numerous electrical related applications ranging from energy storage to sensing, and 3D printing is a promising technique to fabricate such materials with a high degree of freedom and low lead up time. Compared to the existing 3D printing technique for polymer materials, binder jet (BJ) printing offers unique advantages such as a fast production rate, room temperature printing of large volume objects, and the ability to print complex geometries without additional support materials. However, there is a serious lack of research in BJ printing of polymer materials. In this work we introduce a strategy to print poly(vinyl alcohol) composites with MXene-surfactant ink. By ejecting highly conductive MXene particles onto a PVOH matrix, the resulting sample achieved conductive behaviour in the order of mS m^{-1} with demonstrated potential for strain sensing and energy storage. This work demonstrates that BJ printing has the potential to directly fabricate polymer composite materials with different end applications.

Received 21st September 2021
Accepted 20th December 2021

DOI: 10.1039/d1na00698c

rsc.li/nanoscale-advances

1 Introduction

3D printing, also known as Additive Manufacturing (AM), is a rapid process of joining materials layer-by-layer to construct a 3D object with a high degree of freedom, reduced material waste, and short lead up time. Materials such as metals, polymers and ceramics have been successfully printed for different end use applications.[1] Polymer materials are considered as the most common materials used for AM due to the ease of adoption for different printing techniques as well as their wide range of applications including medical treatments,[2] actuators,[3] energy storage devices,[4] various sensors,[5] and energy harvesting devices.[6] There are five main categories of AM for polymers: fused deposition modeling (FMD), powder-liquid printing (PLP), selective laser sintering (SLS), digital light processing (DLP), and robocasting.[7] Due to the intrinsically limited electrical properties of pure polymer materials, there is a demand to print polymer composites for expanded functionalities.[7]

Binder jet (BJ) printing is a type of PLP technique that utilizes inkjet to eject liquid binding agents onto a substrate of powder to form a layer-by-layer cross-sectional structure.[8] Although already commercialized to print sand molds for ceramic casting, study on BJ printing of polymer materials is limited due to the lack of such materials in a fine powder form[9] and robust binding mechanism. Compared to other printing techniques, BJ printing offers unique advantages such as a fast production rate since only the binder material needs to be deposited, single-step production of multi-material objects by switching between multiple inks, room temperature printing of large volume objects, low material waste, and the ability to print hollow structures without any additional support material.[9–12] Most importantly, by introducing functional additives into the ink, BJ printing can directly print polymer composites with desirable electrical properties, which expands BJ printing's potential applications into the field of flexible electronics and Internet of Things (IoT). Therefore, there is great interest in further developing BJ printing of polymer composites with various end functionalities.

Shen *et al.* demonstrated a robust ink deposition system for BJ printing that used a peristaltic pump to eject a continuous stream of water onto poly(vinyl alcohol) (PVOH) powder to form a self-standing 3D structure.[13] To bestow the printed components with electrical functionalities, graphene oxide (GO) was introduced into the ink formulation and the PVOH-GO composite was printed. Multiple reduction methods were then used to reduce GO into reduced graphene oxide (rGO) and achieve printed components with limited electrical conductivity. GO, however, is not a sufficient additive for printing of electronic devices due to the complicated post processing steps required for reduction as well as a low ink concentration of only 0.5 mg mL^{-1}.[12] These led to the printed components with limited electrical performance and a lack of demonstrated applications. Although rGO has the desired electrical properties, its poor dispersion in water limits its ability to be synthesized into a stable ink for printing.[14] A desirable additive for ink

Faculty of Applied Science and Engineering, University of Toronto, Toronto, Ontario, Canada M5S 3G8. E-mail: naguib@mie.utoronto.ca

† Electronic supplementary information (ESI) available. See DOI: 10.1039/d1na00698c

composition therefore requires high intrinsic electrical performance and the ability to easily disperse in aqueous solution.[15–17]

MXenes are a new family of 2D materials that were first discovered in 2011.[18] They are produced from MAX phase precursor with the chemical formula $M_{n+1}AX_n$ where $n = 1$, 2 or 3. M is an early-transition metal such as titanium, A is mostly from Group 13 or 14 of the periodic table, such as aluminum, and X is either carbon or nitrogen.[19] MAX phases form layered hexagonal structures (space group $P6_3/mmc$) of early transition metal carbides with two formula units per cell bond together by the A element. The removal of the A group layer from MAX phases results in a 2D $M_{n+1}X_n$ layer known as MXene, named to denote the loss of the A group and to emphasize its geometrical similarities to graphene.[19] Currently more than 30 MXenes have been discovered with vastly different properties.[18,20] The MXene that received the most attention is the original $Ti_3C_2T_x$ (where T_x represents termination groups such as OH) due to its metallic conductivity,[21] unparalleled volumetric capacitance that is three times higher than those of carbon-based materials,[22] and ability to form a stable colloidal dispersion in water.[23] These unique characteristics make this MXene a favorable additive for inkjet printing, allowing printed components to serve as wireless communication devices,[24] electrophotonic devices,[25] electromagnetic shielding materials,[26] various sensors[27,28] and capacitors.[29–31] However, previous work on inkjet printing of MXenes mostly produced thin films on top of supporting substrates, and printing of a self-standing and flexible 3D structure remains a major challenge.

This work combines the innovative polymer BJ technique with novel 2D $Ti_3C_2T_x$ MXene to print a 3D, flexible and self-standing polymer composite. The hydrophilic surface and negative zeta potential of the MXene in conjunction with our robust ink deposition system allow for the smooth ejection of ultra-high-concentration MXene ink. PVOH is chosen as the polymer material due to its ability to dissolve in water as well as bio-compatibility. For the first time, we show that BJ printing is a viable technique to print functional polymer composites. The printed component is demonstrated as an electrode for micro-capacitors as well as strain sensors. The results of this work could foster new research interest in the field of AM of polymer composites.

2 Experimental section

2.1 Materials

The MAX precursor (Ti_3AlC_2, 200 mesh) was purchased from Forsman Scientific (Beijing, China). Hydrogen chloride (HCl, >99%), sulfuric acid (H_2SO_4, 98%), lithium fluoride (LiF, 99.995%), ethanol (99.9%) and polyethylene glycol *tert*-octylphenyl ether (Triton X-100) were purchased from SigmaAldrich (St Louis, USA). PVOH powder (Product 540s) was purchased from Sekisui Chemical Co., Ltd (Tokyo, Japan).

2.2 MXene ink preparation

$Ti_3C_2T_x$ MXene was synthesized through a minimally intensive layer delamination (MILD) method.[32] 1 g of MAX phase was added over the course of 15 min to a 20 mL aqueous solution of 9 M HCl containing 1.6 g of dissolved LiF. The mixture was stirred at 250 rpm and 35 °C for 48 h. The final dark green colloidal solution was centrifuged at 3500 rpm for 10 min and the supernatant was decanted. The settled MXene was washed with fresh deionized (DI) water repeatedly until the supernatant reached the pH of 6. The resultant colloidal solution was sonicated using a probe sonicator at low settings for 5 min followed by vacuum filtration and vacuum drying at 40 °C for 1 h. The final product was a thick self-standing MXene "cake" with a yield of 90% (Fig. 2c).

The dried MXene was weighed and added to DI water, and diluted Triton X-100 solution at 1 vol% was then added to produce 15 mL of MXene ink. The ink was kept in an ice bath and sonicated with a probe sonicator for 5 min to create a dispersed MXene ink. The ink was stored in a fridge at 4 °C before printing.

2.3 Binder jet printing setup

The BJ printing procedure is described in Fig. 1. The ink reservoir was connected to the ejection nozzle using a polyvinyl chloride (PVC) tube with a 3 mm inner diameter and 5 mm outer diameter. A peristaltic pump was attached to the tube and it generated a continuous jet of ink by spinning at 1600 rpm, resulting in a maximum jet velocity of 2.43 ms^{-1}. The nozzle was suspended 10 mm above the PVOH powder, and the gantry traveled at 15 cm s^{-1} to generate a theoretical resolution of 0.5 mm line width. Ink was injected according to G-Code commands generated from the STL file using Slic3r. After printing, each sample was first washed with ethanol and then dried in a vacuum chamber at 40 °C for 30 min to remove excess water.

2.4 Sample characterization

The electrical conductivities of the MXene cake and printed components were measured using a 4-point probe method with the Alpha-N High Resolution Dielectric Analyzer from Novocontrol Technologies.

A powder X-ray diffractometer (XRD) from Phillip with copper K_α wavelength at 1.5406 Å was used to verify successful etching and exfoliation of the MAX precursor. The geometry and height profile of MXene flakes were analyzed using a Scanning Electron Microscope (SEM) JSM 6060 from JEOL Inc and Atomic Force Microscope (AFM) MultiMode 8-Hr from Bruker by drop casting diluted MXene ink onto a substrate. Zeta potential measurements was performed using MXene ink at 1 mg mL^{-1} with a Nano ZS-ZEN3600 Zetasizer from Malvern. An AR2000 rheometer from TA Instruments was used to measure the rheology of the MXene ink. Thermal gravimetric analysis (TGA) from TA Instruments was used to measure the MXene weight percent in the printed samples by ramping at 20 °C per minute to a target temperature of 700 °C in a nitrogen environment. Ink jet velocity was calculated by measuring the volumetric flow rate of ink with eqn (S1).†

Contact angle measurement of the solution on the powder bed is different from that on a flat continuous surface. The porous structure of the powder bed absorbs solution over time and decreases the contact angle.[33] A 20 μL MXene ink was

dropped onto a flat PVOH powder layer as prepared by the roller of the BJ printer. Approximately 5 to 10 s was given for the ink to reach the meta-stable state before the digital picture was taken. Low-Bond Axisymmetric Drop Shape Analysis (LBADSA) was performed using an ImageJ plugin to fit a contour to the droplet and determine the contact angle.

A two electrode setup was used to characterize the electrochemical performance of printed samples. Two pieces of printed samples each measuring 1 cm^2 and 1 mm thick were used as electrodes and attached to the stainless steel current collector using graphite glue (Ted Pella). The electrodes were separated by a piece of filter paper soaked in 1 M H_2SO_4 which acted as an electrolyte. Measurements were performed using a CHI6054E potentiometer. The capacitance of each electrode was calculated using data from the CV test according to eqn (S2)† and data from the GCD test according to eqn (S3).† The specific capacitance was normalized and reported against the volume of each electrode. Energy stored in capacitors was calculated using eqn (S4),† and the power output was calculated using discharge data from the GCD test. A total of four samples, each printed with different MXene inks, were all subjected to CV, GCD and impedance tests.

Strain sensing properties of the printed samples were studied using an Instron Microtester 5848 with a 500 N loading cell by cyclic tensile stretching. Resistance changes were obtained using a National Instrument 6210-USB Analog DAQ box, with 5 V supply from an Arduino Uno, as shown in Fig. S8.† Data were acquired and analyzed using MATLAB/Simulink 2019a. A total of three samples were used for strain sensing measurements, one for each sub-figure of Fig. 7. The initial resistance of the sample was measured as 63 Ωm.

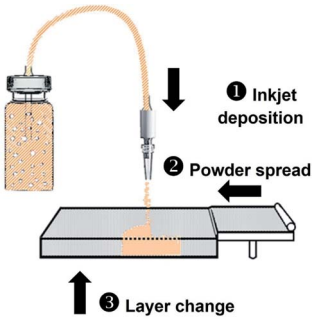

Fig. 1 Illustration of the BJ printing process. MXene ink supply was connected to a peristaltic pump and print nozzle to form an inkjet setup. A roller distributed an even layer of PVOH powder onto the print stage. The pump then generated a Continuous Jet (CJ) of MXene ink at a top speed of 2.43 ms^{-1} directly onto PVOH powder, which first dissolved and then physically crosslinked to retain its geometry as water evaporated. The printing bed was lowered and the process was repeated until the final 3D part was obtained.

Table 1 Summary of literature on MXene ink printing *via* inkjet DOD

MXene ink ($mg\ mL^{-1}$)	Description	Ref.
0.5	Proof of concept	37
1	Hydrogen peroxide sensor	28
1	Oxidation resistance of MXene	30
1	Proof of concept	38
2	Broadband ultrafast photonic applications	25
2	Electrodes for bio-sensing	27
2.25	Electrode	26
12	CJ inkjet printing	This work

3 Results and discussion

3.1 Development of MXene ink

A weakly bonded aluminum layer sandwiched between two layers of titanium carbide MAX precursor (Ti_3AlC_2) was chemically etched to form MXene ($Ti_3C_2T_x$).[18] Successful etching was confirmed *via* XRD (Fig. 2a). The characteristic peak of the MAX phase precursor at 38° was flattened, indicating successful and complete conversion to multi-layered MXene with a flake thickness of 20 nm (Fig. S1†). The resulting material was a self-standing MXene cake (Fig. 2c). The electrical conductivity of MXene from this work was measured to be 4.9×10^4 S m^{-1}, higher than that of rGO with a conductivity of 2.7×10^4 S m^{-1}.[34] MXene demonstrated a graphene-like flake morphology with a lateral dimension of 5 μm (Fig. 2d).

Ink concentration is a fundamental factor for the electrical performance of printed components as a higher additive concentration theoretically creates better interconnected electrical networks, leading to the percolation threshold.[35] However, for inkjet technologies, the 2D additive in the ink was limited to below 50 $mg\ mL^{-1}$ (5 wt%) in order to maintain a printable viscosity and flow rate.[36] Aqueous MXene ink accommodates even lower concentration due to the clay-like behaviour of MXene. Table 1 summarizes the Drop on Demand (DOD) aqueous MXene ink concentration using inkjet technology, and the maximum achievable concentration was only 2.25 $mg\ mL^{-1}$.

The robustness of the CJ system used in this work could tolerate inks with a wider window of properties.[13] Other studies on the rheological properties of MXene ink also confirmed that the electrostatic force of the MXene flake should allow for higher solid concentration.[39] In this work the maximum MXene concentration was set at 12 $mg\ mL^{-1}$, which is nearly five times higher than those of other studies summarized in Table 1. Further increasing the MXene concentration would lead to unreliable formation of a stable CJ. The lower bound was set at 0.5 $mg\ mL^{-1}$ to investigate the change in the electrical and electrochemical performance of the printed components with increasing ink concentration.

The hydrophilic surface of MXene flakes has a tendency to attract water molecules away from the PVOH substrate and create large contact angles due to the high surface tension (Fig. 3a). This not only inhibited the wetting interaction between ink and powder, but also resulted in elastic collision which deviated ink from landing at the target site. The results were sections of the printed component not saturated with ink (Fig. S4 and S5†). These voids were detrimental to material properties, as the printed components would exhibit lower mechanical strength and lower electrical performance after

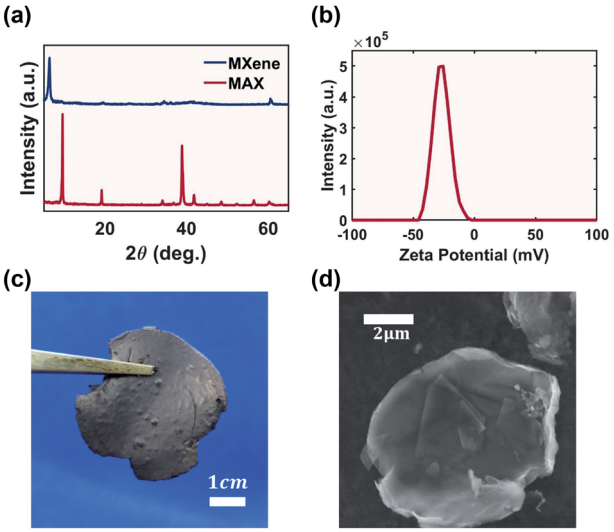

Fig. 2 Characterization of the synthesized MXene: (a) XRD patterns of the MAX precursor and MXene; (b) zeta potential measurement of MXene; (c) self-standing MXene cake; and (d) SEM image of the multi-layered MXene flake.

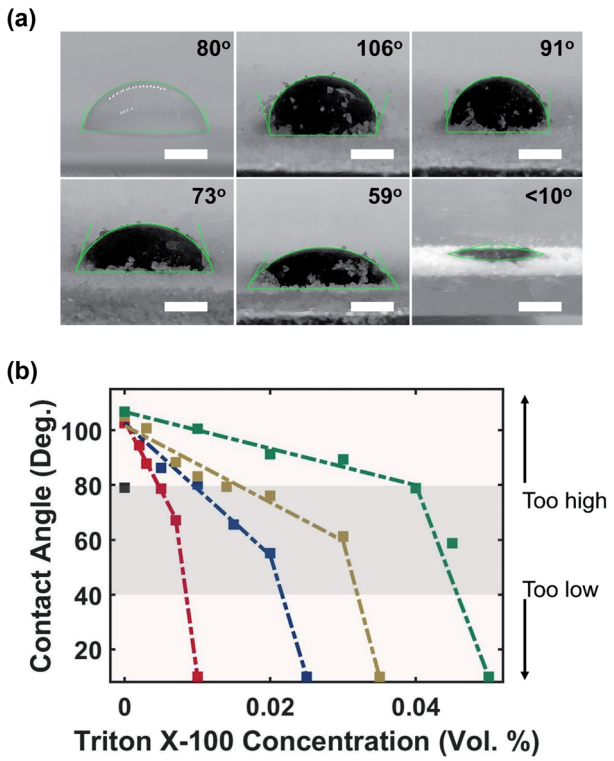

Fig. 3 (a) Change in the contact angle of 12 mg mL^{-1} MXene ink as surfactant concentration was increased. Order from left to right: water, 0 vol%, 0.2 vol%, 0.3 vol%, 0.45 vol% and 0.50 vol%. The scale bars correspond to 1 mm; (b) contact angle of various MXene-surfactant ink on a PVOH powder substrate. Red: 0.5 mg mL^{-1}, blue: 4 mg mL^{-1}, yellow: 8 mg mL^{-1} and green: 12 mg mL^{-1}. Shaded region indicates the suitable contact angle range as determined by using water as the benchmark. All ink compositions in the shaded region have been tested to successfully print continuous components.

drying. To ensure a favorable ink–powder interaction, Triton X-100 was added as a surfactant to tune the ink's surface tension. Triton X-100 is a non-ionic surfactant; it has been used previously to decrease the surface energy of MXene ink and also suppress the weak Marangoni flow which can reduce the coffee-ring effect.[30] Triton X-100 molecules adsorb onto MXene particles to form a steric barrier which reduces MXene's hydrophilic behaviour, improving ink–powder interactions.[40]

Fig. 3b shows the relationship between the surfactant concentration and contact angle. With only 0.5 mg mL^{-1} (0.05 wt%) of MXene, the contact angle increased sharply from 80° (water) to 115°, and further increasing the MXene concentration had no impact with a stable contact angle in the range of (110 ± 5)°. Introducing the surfactant immediately reduced the contact angle, and the rate of decrease was slower for ink with higher MXene concentration, as evidenced by the shallower slope. Further increasing the surfactant concentration after the saturation point sharply decreased the contact angle to approximately 10° as shown by the sharper slope. Fig. 3a shows a gradual reduction in the contact angle of 12 mg mL^{-1} MXene ink as the surfactant concentration was increased.

By adjusting the surfactant concentration to maintain a contact angle in the range of (60 ± 20)°, MXene-surfactant ink can print continuous and uniform lines with a width of (2.2 ± 0.3) mm (Fig. S4†) and void free samples (Fig. S6†). The contact angle higher than 80° led to elastic collision and a contact angle lower than 20° led to excessive spreading which significantly increased the line width. The final ink compositions were: 0.01 vol% surfactant at 0.5 mg mL^{-1} concentration, 0.02 vol% surfactant at 4 mg mL^{-1} concentration, 0.03 vol% surfactant at 8 mg mL^{-1} concentration, and finally 0.045 vol% surfactant at 12 mg mL^{-1} concentration.

3.2 Characterization of MXene ink

Achieving a stable dispersion of additives in liquid medium is a key criterion for ink formulation.[17] Unstable ink results in agglomeration of additives in the printed components, reducing electrical performance. One criterion that governs the dispersion of nano-additives is their zeta potential. Typically a potential of −30 mV could prevent aggregation due to the repulsion forces between nano-particles. The zeta potential of MXene is measured as −29 mV (Fig. 2b), which is adequate to form a stable dispersion at a high MXene concentration of 12 mg mL^{-1}.

MXene-surfactant inks were able to maintain quasi-stable dispersion after two weeks with minimal visually observable agglomeration (Fig. S2†). The only exception was with 0.5 mg mL^{-1} ink, where all the MXene aggregated and settled. This was due to the low concentration of MXene present. Although higher ink concentration had proportionally higher settling at the bottom of the vial due to the restacking of MXene flakes, the darker color suggested that they still had more dispersed MXene flakes. Regardless, of all concentrations the aggregated MXene could be re-dispersed *via* vigorous hand shaking (Fig. S3†).

Rheology tests were performed to verify that ink at such high concentration still behaved as a colloidal liquid dispersion

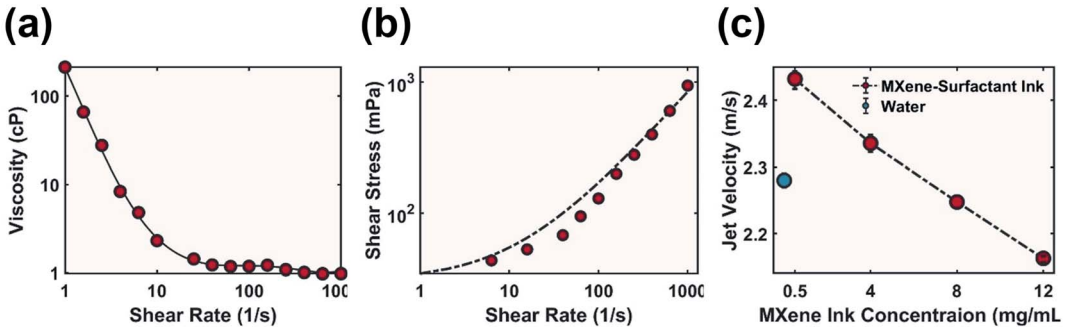

Fig. 4 (a) and (b) are for MXene-surfactant ink at 12 mg mg L^{-1}. (a) Dynamic viscosity result showing a shear thinning effect. (b) Herschel–Bulkley model (dashed line). $n = 0.76$, $k = 4.22$ and $\tau_0 = 0.35$. (c) Jet velocity of MXene-surfactant ink.

instead of a cement-like paste typical for clay materials such as MXene. Ink demonstrated shear thinning behaviour (Fig. 4a) as viscosity decreased when increasing the shear rate, which would aid in sustaining a smooth flow out of a narrow nozzle.[41] This behaviour was also confirmed by fitting the shear stress data to the Herschel–Bulkley model for non-Newtonian fluid (Fig. 4b and eqn (S5)†). 12 mg mL^{-1} MXene-surfactant ink had a flow index $n < 1$, implying desirable shear thinning above a yield stress.[42] The ink viscosity was also an order of magnitude lower than that of higher concentration ink used for direct ink writing, which is typical for inkjet printable ink.[38,43]

Although the MXene-surfactant ink at various MXene concentrations had approximately identical surface energy, an increase in MXene concentration (and thus an increase in surfactant concentration) led to a decrease in jet velocity (Fig. 4c). This behaviour was likely due to an increase in ink viscosity as at the same pressure difference (pump set to constant 1600 rpm) thicker fluids flow more slowly. The ink ejection speed allowed good penetration into the powder substrate, improved ink–powder interaction, and benefited liquid behaviour of the ink to promote shear thinning.

To guarantee smooth ink ejection without clogging, the lateral dimension of the additive must be 1/50 the inner diameter of the print nozzle.[36,44,45] MXene flakes had a lateral diameter between 2 and 5 μm (Fig. S3†), and therefore a stainless steel Gauge 25 needle with an inner diameter of 260 μm was chosen. Shear stress of ink during ejection was calculated with eqn (S6),† and a high shear stress of 2.07×10^4 mPa was achieved with MXene-surfactant ink at 12 mg mL^{-1}. This is five orders of magnitude higher than the ink's yield stress (Fig. 4b), which further proves shear thinning behaviour during ejection. Continuous and void-free samples were repeatedly printed without clogging (Fig. S6†). The printed sample also demonstrated excellent elastic deformation capability, and the ability to be stretched (Fig. 5b), twisted (Fig. 5c) and bent (Fig. 5d).

3.3 Composition and electrical analysis

The electrical performance of the composite material is partially dictated by additive concentration and distribution. MXene wt% in the printed components increased with respect to increasing ink concentration (Fig. 6a). This relationship is not linear due to the decrease in ink flow rate as evidenced by the decrease in jet velocity (Fig. 4c and eqn (S1)†). Increasing the ink concentration 24 times increased MXene wt% more than six times, and increased the conductivity by five orders of magnitude to 25.4 mS m^{-1} (Fig. 6a). The ratio of conductivity to loading $\left(\frac{\sigma}{\text{wt\%}}\right)$ is nearly identical to that of the MXene/polyacrylamide composite fabricated by solution casting.[46] Table 2 compares the MXene wt% and respective conductivity values of the reported MXene/polymer composites. MXene wt% of the printed sample was limited to below 5 wt%, lower than that of the MXene composite fabricated *via* solvent casting and the vacuum assisted filtration (VAF) method.

To ensure the formation of continuous conductive pathways, many studies relied on embedding pure MXene-film layers in between insulating polymer layers.[47,48] In comparison, Ling *et al.* and Lipton *et al.* both fabricated PVOH-MXene composites at around 40 wt% MXene loading. By embedding MXene as a pure film Lipton *et al.* achieved a conductivity more than 3000

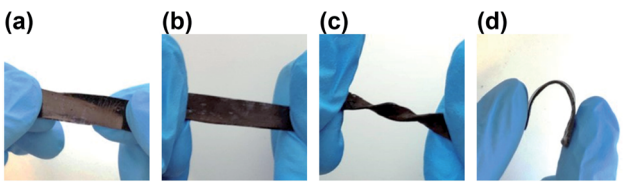

Fig. 5 (a) Printed rectangular sample measuring 4 cm × 1 cm × 1 mm; (b) stretched by hand to approximately 50% strain; (c) twisted and (d) bent with a radius of curvature of 0.46 cm.

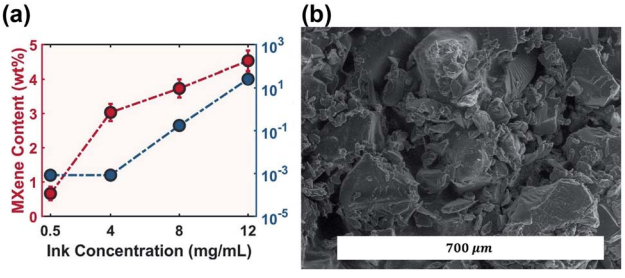

Fig. 6 (a) MXene wt% and conductivity of printed samples; (b) SEM image on the surface of the printed sample using MXene-surfactant ink at 12 mg mL^{-1}.

Table 2 Summary of electrical conductivity and MXene wt% values of reported MXene/polymeric composites

MXene loading (wt%)	Conductivity (S m^{-1})	Description	Ref.
0.14	5.9×10^{-2}	Electrospun PVOH nano-fiber decorated with MXene	49
1	1	Electrospun polyurethane fibre with the MXene shell	51
4.53	2.5×10^{-2}	Binder jet printed	This work
6	3.3×10^{-2}	Solution cast MXene and polyacrylamide film	46
10	1.26×10^{-2}	VAF MXene and PVOH film	52
19.5	716	Sandwich structured MXene and PVOH film	48
40	4×10^{-2}	VAF MXene and PVOH film	21
45.5	53–125	Sandwich structured MXene, clay and PVOH film	47
50	1.26×10^{2}	VAF MXene and PVOH film	52
87.5	3.4×10^{4}	VAF MXene and PEDOT : PSS film	50

times higher than that reported by Ling *et al.*, who evenly distributed MXene in the sample *via* VAF.[21,47] The highest conductivity to wt% ratio of evenly distributed MXene with a non-conducting polymer was achieved by Sobolciak *et al.*, in which only 0.14 wt% of MXene was decorated onto an electrospun PVOH nano-fiber to achieve a conductivity of 5.9×10^{-2} S m^{-1}. SEM imaging showed even distribution of MXene on the fiber which formed conductive pathways.[49] These analyses provide insights into strategies for better conductivity of MXene based composites. However, all of the above techniques required top-down methods with multiple synthesis steps, whereas BJ printing used in this work is a bottom-up method which could directly print PVOH-MXene composites.

Based on the results from this work and comparison against Table 2, it is found that a higher MXene ink concentration is required to further improve electrical conductivity. However, the MXene ink concentration was dictated by ink rheology, and further improving the concentration would make ink unprintable due to the increased viscosity and higher likelihood of nozzle clogging. Therefore, there is great interest for future work to develop higher MXene concentration ink that could be ejected without obstruction by the inkjet CJ method. The highest conductivity to wt% ratio in Table 2 was achieved with the MXene/poly(3,4-ethylenedioxythiophene) polystyrene sulfonate (PEDOT : PSS) composite.[50] PEDOT : PSS is an intrinsically conductive polymer, which is effective in bridging a conductive path between MXene flakes. PEDOT : PSS not only could be dispersed in water medium,[4] but could also be synthesized into a dry pellet form. Thus, future work in BJ printing could utilize PEDOT : PSS powder as a polymer material to be printed with aqueous based MXene ink for high performance electronic materials.

3.4 Tensile strain sensor

MXene has been recently demonstrated as a viable additive for strain sensors as the migration of particles leads to resistance variation.[53,54] To demonstrate potential applications of the printed components, an ASTM Type V tensile testing specimen printed with MXene-surfactant ink at 12 mg mL^{-1} was used as a sensor to detect tensile strain in gauge length.

Multiple strains were applied to the sample with relaxation time in between (Fig. 7a). Strain as high as 250% was detected. The sample experienced plastic deformation above 50% resulting in an increased response during full relaxation. However, the printed component was suitable to sense cyclic deformation at a low strain of 50% with minimum hysteresis as the peak signal and the signal during relaxation were relatively consistent after ten cycles (Fig. 7b). The sample also retained structural integrity after prolonged strain cycles (Fig. S9†). The response time of the material was consistently below 0.5 s as the peak force was synchronized with the peak signal.

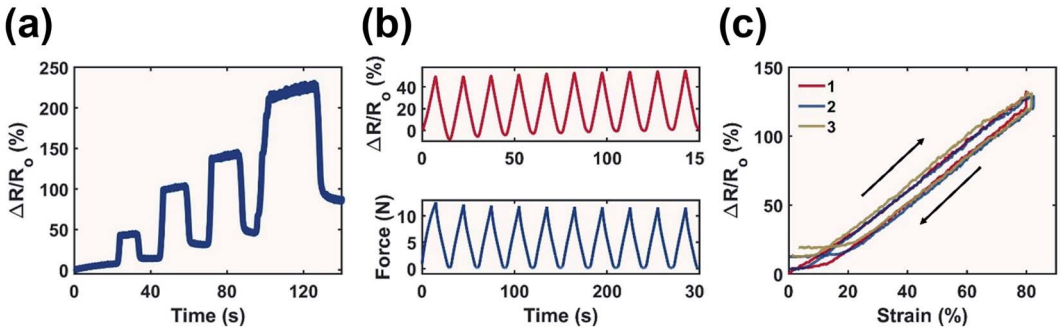

Fig. 7 Printed sample with MXene-surfactant ink at 12 mg mL^{-1} tested as a strain sensor: (a) demonstrating a change in resistance proportional to various changes in elongation at an extension rate of 2 mm s^{-1}. The four peaks correspond to 50%, 125%, 165% and 250% strain respectively; (b) 10 cycles of 50% strain at 1 mm s^{-1} and (c) the linear relationship of three stretching cycles between the signal response and applied strain at 0.03% s^{-1} during the stretching (arrow up) and relaxation (arrow down) phase.

The plastic deformation experienced by the printed sample at ≥50% strain led to an increase in the minimal detection threshold over repeated strain cycles (Fig. 7c). While during the first cycle the output signal increased linearly with respect to strain immediately after strain application, during the second and third cycles the signal only started to increase after 5.5% and 9.0% strain respectively. A similar observation was true during the relaxation phase, where the minimal detectable strain increased from 12.7% during the first cycle to 19.6% and 22.4% for the second and third cycles. This is evident by the flattened response curve in Fig. 7c at low strain, as the buckling of the printed sample neutralized applied strain, resulting in zero change in gauge length.

Most importantly, the printed material demonstrated a linear relationship between the signal response and applied strain during the stretching and relaxation phase between 0% and 80% strain (Fig. 7c). This led to a consistent Gauge Factor (GF, eqn (S7)†) which is desirable for strain detection as the signal response could be accurately and effortlessly converted to reflect the applied strain. The calculated GF was also consistent between repeated strain. A GF of 1.65 ± 0.16 was recorded during the stretching phase of three repeated cycles, and it only increased marginally during the relaxation phase to 1.69 ± 0.3. This implies that the printed material is reliable for strain detection for both stretching and relaxation. The GF of this work is comparable against those of other MXene based tensile sensors. Liao *et al.* combined MXene with an organohydrogel and reported a GF of 5.02 at <200% strain,[55] Yang *et al.* used MXene to develop hierarchical morphologies on piezoresistive layers and reported a GF of close to 1 at <80% strain.[56] The main advantage of this work is the demonstrated consistent GF at <80% strain especially during the first cycle strain application. This is a rather unique characteristic compared to other MXene based tensile sensors from recent studies, which all demonstrated a change in GF at <80% strain.[57–61]

3.5 Electrochemical properties

The rough surface features of the printed sample (Fig. 6b) could theoretically allow for additional charge storage sites to improve capacitance compared to a flat surface. The cyclic voltammograms (Fig. 8a) demonstrated a mix of blunt and slanted profile, which is typical for printed capacitors consisting of both conductive and non-conductive materials.[62] This profile indicated the existence of both series resistance (ESR) due to the resistance of the MXene electrode as well as parallel resistance (EPR) from finite conduction through the electrolyte.[63] The anodic peak discharge current density increased from 1.38 mA cm^{-3} to 2.82 mA cm^{-3} when the ink concentration was increased 24 times (Fig. 8b), which corresponded to an increase in capacitance. At a scan rate of 5 mV s^{-1} the specific capacitance of the electrode increased eight times from 2.5 to 20.05 mF cm^{-3} with increasing MXene ink concentration (Fig. 8d). Capacitance decreased when the scan rate was increased from 5 to 1000 mV s^{-1} (Fig. 8e), which was potentially due to the relatively high resistance of the electrode,[38] as well as the non-porous surface (Fig. 6b) which inhibited the accessibility of

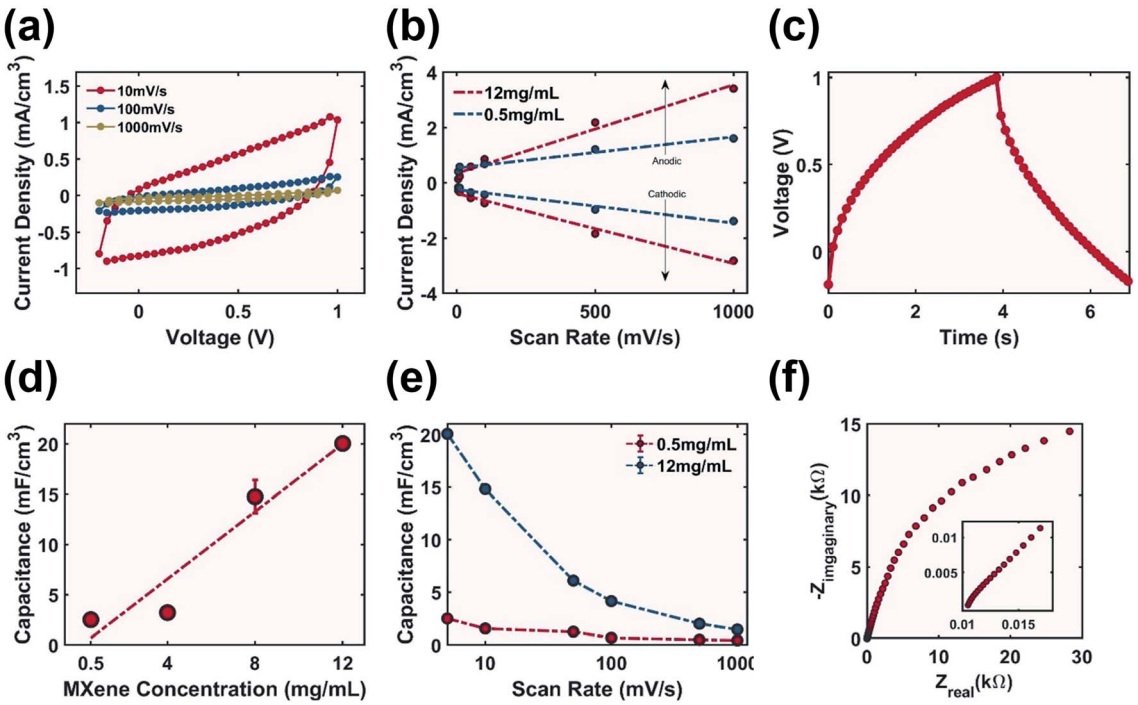

Fig. 8 Electrochemical performance with 1 M H_2SO_4 electrolyte: (a) CV curve for the sample printed with 12 mg mL^{-1} MXene-surfactant ink; (b) cell peak current density; (c) charge–discharge curve of the sample printed with 12 mg mL^{-1} MXene-surfactant ink at a charging rate of 50 μA cm^{-2}; (d) capacitance of printed samples at 5 mV s^{-1}; (e) change in capacitance as a function of scan rate and (f) the Nyquist plot with ESR = 10.5 Ω.

ions in the electrodes resulting in rate performance that could be further improved.[64]

The Nyquist plot (Fig. 8f) of the electrode printed with 12 mg mL^{-1} MXene-surfactant ink had an ESR of 10.5 Ω indicating that the cell setup could be optimized by improving the electrode–electrolyte contact. No semi-circle was observed in the high frequency range indicating no contribution from charge transfer resistance (R_{CT}). The slope in the high frequency range was close to 0.83 (inset of Fig. 8f), and the imaginary impedance from capacitance slowly increased in the low frequency range. This could be due to the low conductivity of the electrode not allowing all reactive sites to be fully accessible in a short time as well as inefficient porous electrode behaviour.[62]

The GCD test was performed using samples printed with 12 mg mL^{-1} MXene-surfactant ink at a charge rate of 50 μA cm^{-2}. The charge time of 3.85 s and discharge time of 3.02 s were observed (Fig. 8c). After 100 cycles of charge–discharge the capacity retention stabilized at 80% (Fig. S10†), and this decrease could be due to the parasitic reaction of the electrolyte dissolving the electrode. Using GCD data the calculated specific capacitance of the electrode was 20.76 mF cm^{-3} (eqn (S3)†) with an energy density of 14.95 mJ cm^{-3} (eqn (S4)†) and a power density of 4.95 mW cm^{-3}.

The BJ printed PVOH-MXene electrode demonstrated similar areal capacitance across a wide range of scan rates and current densities as to interdigital MXene film capacitors reported in the literature. Zhang *et al.* first used the stamping method on various substrates such as polyethylene terephthalate (PET) and paper to achieve a peak capacity of 61 mF cm^{-2};[65] later Zhang *et al.* used inkjet printing on the PET substrate and showed that by increasing the number of print passes from 1 to 5, the capacity increased correspondingly from 3.5 to 43 mF cm^{-2}.[37] Yu *et al.* also reported a similar performance of below 20 mF cm^{-2} for inkjet printed MXene film capacitors.[66] Due to the limited MXene content, the areal capacity of the printed component from this work is lower than that of the extrusion printed MXene 3D capacitor which can reach a capacity in the order of 1 F cm^{-2}.[41,67]

To the best of the authors' knowledge, this work is the first to use the MXene-PVOH composite as an electrode material for capacitors, whereas other studies utilized pure MXene *via* the inkjet or extrusion method. Without insulating binding materials these electrodes could achieve metallic conductivity, allowing them to be fabricated into interdigital electrochemical capacitors by serving as both the electrode and the current collector.[67] The low MXene content of less than 5 wt% in this work compared to other studies with the pure MXene electrode translated to fewer charge storage sites. However, the advantage of BJ printing is that a self-standing and flexible electrode with a 3D structure could be printed, whereas all the other methods typically require a separate substrate to retain structural stability.[37]

4 Conclusion

In this work a MXene ink at 12 mg mL^{-1} was formulated with Triton-X 100 surfactant for BJ 3D printing. Rheology measurements showed that at this high concentration, ink still behaved as a liquid with excellent shear thinning behaviour, thus allowing for printing of a continuous and void free PVOH composite. Furthermore, increasing ink concentration is shown as an effective strategy to improve the electrical and electrochemical performance of BJ printed components. For the first time, the BJ technique was used to print a polymer composite with different end applications. The printed component was demonstrated as both a strain sensor and an electrode for micro-capacitors. The result of this work could not only foster new research interest in the area of BJ printing, but also inspire development of new 3D printing techniques for polymer composites.

Author contributions

Terek Li: conceptualization, methodology, validation, formal analysis, writing – original draft. Tianhao Chen: methodology, validation, writing – review & editing. Xuechen Shen: methodology, validation, writing – review & editing. HaoTian Harvey Shi: methodology, writing – review & editing. Elahe Jabari: conceptualization, data curation. Hani E. Naguib: conceptualization, writing – review & editing, supervision.

Conflicts of interest

There are no conflicts to declare.

Acknowledgements

The authors would like to acknowledge the financial support of the Natural Science and Engineering Research Council of Canada (NSERC) and the NSERC Network for Holistic Innovation in Additive Manufacturing (HI-AM).

Notes and references

1 T. D. Ngo, A. Kashani, G. Imbalzano, K. T. Nguyen and D. Hui, *Composites, Part B*, 2018, **143**, 172–196.
2 G. Basara, M. Saeidi-Javash, X. Ren, G. Bahcecioglu, B. C. Wyatt, B. Anasori, Y. Zhang and P. Zorlutuna, *Acta Biomater.*, 2020, DOI: 10.1016/j.actbio.2020.12.033.
3 G. Grau, E. J. Frazier and V. Subramanian, *Microsyst. Nanoeng.*, 2016, **2**, 1–8.
4 H. Yuk, B. Lu, S. Lin, K. Qu, J. Xu, J. Luo and X. Zhao, *Nat. Commun.*, 2020, **11**, 4–11.
5 B. Shih, C. Christianson, K. Gillespie, S. Lee, J. Mayeda, Z. Huo and M. T. Tolley, *Front. Robot. AI*, 2019, **6**, 1–12.
6 X. Yuan, X. Gao, J. Yang, X. Shen, Z. Li, S. You, Z. Wang and S. Dong, *Energy Environ. Sci.*, 2020, **13**, 152–161.
7 J. Saroia, Y. Wang, Q. Wei, M. Lei, X. Li, Y. Guo and K. Zhang, *Int. J. Adv. Des. Manuf. Technol.*, 2020, **106**, 1695–1721.
8 A. Azhari, E. Marzbanrad, D. Yilman, E. Toyserkani and M. A. Pope, *Carbon*, 2017, **119**, 257–266.
9 M. Ziaee and N. B. Crane, *Addit. Manuf.*, 2019, **28**, 781–801.

10 A. Mostafaei, A. M. Elliott, J. E. Barnes, F. Li, W. Tan, C. L. Cramer, P. Nandwana and M. Chmielus, *Prog. Mater. Sci.*, 2020, **100**, 707.
11 Y. Wang, Z. Xu, D. Wu and J. Bai, *Materials*, 2020, **13**, 2406.
12 X. Shen, M. Chu, F. Hariri, G. Vedula and H. E. Naguib, *Addit. Manuf.*, 2020, **36**, 101–565.
13 X. Shen and H. E. Naguib, *Addit. Manuf.*, 2019, **29**, 100–820.
14 A. Ciesielski and P. Samorì, *Chem. Soc. Rev.*, 2014, **43**, 381–398.
15 L. Nayak, S. Mohanty, S. K. Nayak and A. Ramadoss, *J. Mater. Chem. C*, 2019, **7**, 8771–8795.
16 E. Jabari, F. Ahmed, F. Liravi, E. B. Secor, L. Lin and E. Toyserkani, *2D Mater.*, 2019, **6**, 042004.
17 M. Gao, L. Li and Y. Song, *J. Mater. Chem. C*, 2017, **5**, 2971–2993.
18 M. Naguib, M. Kurtoglu, V. Presser, J. Lu, J. Niu, M. Heon, L. Hultman, Y. Gogotsi and M. W. Barsoum, *Adv. Mater.*, 2011, **23**, 4248–4253.
19 M. Naguib, J. Come, B. Dyatkin, V. Presser, P.-L. Taberna, P. Simon, M. W. Barsoum and Y. Gogotsi, *Electrochem. Commun.*, 2012, **16**, 61–64.
20 J. L. Hart, K. Hantanasirisakul, A. C. Lang, B. Anasori, D. Pinto, Y. Pivak, J. T. van Omme, S. J. May, Y. Gogotsi and M. L. Taheri, *Nat. Commun.*, 2019, **10**, 522.
21 Z. Ling, C. E. Ren, M. Q. Zhao, J. Yang, J. M. Giammarco, J. Qiu, M. W. Barsoum and Y. Gogotsi, *Proc. Natl. Acad. Sci. U. S. A.*, 2014, **111**, 16676–16681.
22 M. Ghidiu, M. R. Lukatskaya, M.-Q. Zhao, Y. Gogotsi and M. W. Barsoum, *Nature*, 2014, **516**, 78–81.
23 O. Mashtalir, M. Naguib, V. N. Mochalin, Y. Dall'Agnese, M. Heon, M. W. Barsoum and Y. Gogotsi, *Nat. Commun.*, 2013, **4**, 1–7.
24 A. Sarycheva, A. Polemi, Y. Liu, K. Dandekar, B. Anasori and Y. Gogotsi, *Sci. Adv.*, 2018, **4**, 1–9.
25 X. Jiang, W. Li, T. Hai, R. Yue, Z. Chen, C. Lao, Y. Ge, G. Xie, Q. Wen and H. Zhang, *npj 2D Mater. Appl.*, 2019, **3**, 34.
26 M. Vural, A. Pena-Francesch, J. Bars-Pomes, H. Jung, H. Gudapati, C. B. Hatter, B. D. Allen, B. Anasori, I. T. Ozbolat, Y. Gogotsi and M. C. Demirel, *Adv. Funct. Mater.*, 2018, **28**, 1–10.
27 A. Saleh, *J. Phys.: Mater.*, 2020, **3**, 044004.
28 J. Zheng, J. Diao, Y. Jin, A. Ding, B. Wang, L. Wu, B. Weng and J. Chen, *J. Electrochem. Soc.*, 2018, **165**, B227–B231.
29 C. J. Zhang, S. H. Park, A. Seral-Ascaso, S. Barwich, N. McEvoy, C. S. Boland, J. N. Coleman, Y. Gogotsi and V. Nicolosi, *Nat. Commun.*, 2019, **10**, 849.
30 C. W. Wu, B. Unnikrishnan, I. W. P. Chen, S. G. Harroun, H. T. Chang and C. C. Huang, *Energy Storage Mater.*, 2020, **25**, 563–571.
31 S. Uzun, M. Schelling, K. Hantanasirisakul, T. S. Mathis, R. Askeland, G. Dion and Y. Gogotsi, *Small*, 2021, **17**, 1–12.
32 M. Alhabeb, K. Maleski, B. Anasori, P. Lelyukh, L. Clark and S. Sin, 2017.
33 Y. Bai, C. Wall, H. Pham, A. Esker and C. B. Williams, *J. Manuf. Sci. Eng.*, 2019, **141**, 1–11.
34 C. M. Chen, J. Q. Huang, Q. Zhang, W. Z. Gong, Q. H. Yang, M. Z. Wang and Y. G. Yang, *Carbon*, 2012, **50**, 659–667.
35 S. Tu, Q. Jiang, X. Zhang and H. N. Alshareef, *ACS Nano*, 2018, **12**, 3369–3377.
36 G. Hu, J. Kang, L. W. Ng, X. Zhu, R. C. Howe, C. G. Jones, M. C. Hersam and T. Hasan, *Chem. Soc. Rev.*, 2018, **47**, 3265–3300.
37 C. J. Zhang, L. McKeon, M. P. Kremer, S. H. Park, O. Ronan, A. Seral-Ascaso, S. Barwich, C. Coileáin, N. McEvoy, H. C. Nerl, B. Anasori, J. N. Coleman, Y. Gogotsi and V. Nicolosi, *Nat. Commun.*, 2019, **10**, 1–9.
38 E. Quain, T. S. Mathis, N. Kurra, K. Maleski, K. L. Van Aken, M. Alhabeb, H. N. Alshareef and Y. Gogotsi, *Adv. Mater. Technol.*, 2019, **4**, 1–7.
39 B. Akuzum, K. Maleski, B. Anasori, P. Lelyukh, N. J. Alvarez, E. C. Kumbur and Y. Gogotsi, *ACS Nano*, 2018, **12**, 2685–2694.
40 A. Sharipova, S. Aidarova, B. Mutaliyeva, A. Babayev, M. Issakhov, A. Issayeva, G. Madybekova, D. Grigoriev and R. Miller, *Colloids Interfaces*, 2017, **1**, 3.
41 J. Orangi, F. Hamade, V. A. Davis and M. Beidaghi, *ACS Nano*, 2020, **14**, 640–650.
42 G. Chauhan, A. Verma, A. Das and K. Ojha, *Rheol. Acta*, 2018, **57**, 287–291.
43 A. Russo, B. Y. Ahn, J. J. Adams, E. B. Duoss, J. T. Bernhard and J. A. Lewis, *Adv. Mater.*, 2011, **23**, 3426–3430.
44 K. Parvez, R. Worsley, A. Alieva, A. Felten and C. Casiraghi, *Carbon*, 2019, **149**, 213–221.
45 F. Torrisi, T. Hasan, W. Wu, Z. Sun, A. Lombardo, T. S. Kulmala, G. W. Hsieh, S. Jung, F. Bonaccorso, P. J. Paul, D. Chu and A. C. Ferrari, *ACS Nano*, 2012, **6**, 2992–3006.
46 M. Naguib, T. Saito, S. Lai, M. S. Rager, T. Aytug, M. Parans Paranthaman, M. Q. Zhao and Y. Gogotsi, *RSC Adv.*, 2016, **6**, 72069–72073.
47 J. Lipton, G. M. Weng, M. Alhabeb, K. Maleski, F. Antonio, J. Kong, Y. Gogotsi and A. D. Taylor, *Nanoscale*, 2019, **11**, 20295–20300.
48 X. Jin, J. Wang, L. Dai, X. Liu, L. Li, Y. Yang, Y. Cao, W. Wang, H. Wu and S. Guo, *Chem. Eng. J.*, 2020, **380**, 122475.
49 P. Sobolčiak, A. Ali, M. K. Hassan, M. I. Helal, A. Tanvir, A. Popelka, M. A. Al-Maadeed, I. Krupa and K. A. Mahmoud, *PLoS One*, 2017, **12**, DOI: 10.1371/journal.pone.0183705.
50 R. Liu, M. Miao, Y. Li, J. Zhang, S. Cao and X. Feng, *ACS Appl. Mater. Interfaces*, 2018, **10**, 44787–44795.
51 S. Seyedin, S. Uzun, A. Levitt, B. Anasori, G. Dion, Y. Gogotsi and J. M. Razal, *Adv. Funct. Mater.*, 2020, **30**, 1–11.
52 T. Habib, X. Zhao, S. A. Shah, Y. Chen, W. Sun, H. An, J. L. Lutkenhaus, M. Radovic and M. J. Green, *npj 2D Mater. Appl.*, 2019, **3**, 1–6.
53 Y. Yang, L. Shi, Z. Cao, R. Wang and J. Sun, *Adv. Funct. Mater.*, 2019, **29**, 1–10.
54 Y. Z. Zhang, K. H. Lee, D. H. Anjum, R. Sougrat, Q. Jiang, H. Kim and H. N. Alshareef, *Sci. Adv.*, 2018, **4**, 1–8.
55 H. Liao, X. Guo, P. Wan and G. Yu, *Adv. Funct. Mater.*, 2019, **29**, 1–9.
56 H. Yang, X. Xiao, Z. Li, K. Li, N. Cheng, S. Li, J. H. Low, L. Jing, X. Fu, S. Achavananthadith, F. Low, Q. Wang,

P. L. Yeh, H. Ren, J. S. Ho, C. H. Yeow and P. Y. Chen, *ACS Nano*, 2020, **14**, 11860–11875.
57 M. Chao, Y. Wang, D. Ma, X. Wu, W. Zhang, L. Zhang and P. Wan, *Nano Energy*, 2020, **78**, 105187.
58 H. Li and Z. Du, *ACS Appl. Mater. Interfaces*, 2019, **11**, 45930–45938.
59 Y. Yang, L. Shi, Z. Cao, R. Wang and J. Sun, *Adv. Funct. Mater.*, 2019, **29**, 1–10.
60 X. Shi, H. Wang, X. Xie, Q. Xue, J. Zhang, S. Kang, C. Wang, J. Liang and Y. Chen, *ACS Nano*, 2019, **13**, 649–659.
61 Y. Cai, J. Shen, G. Ge, Y. Zhang, W. Jin, W. Huang, J. Shao, J. Yang and X. Dong, *ACS Nano*, 2018, **12**, 56–62.
62 T. S. Mathis, N. Kurra, X. Wang, D. Pinto, P. Simon and Y. Gogotsi, *Adv. Energy Mater.*, 2019, **9**, 1–13.
63 D. Boonpakdee, C. F. Guajardo Yévenes, W. Surareungchai and C. La-O-Vorakiat, *J. Mater. Chem. A*, 2018, **6**, 7162–7167.
64 X. Gao and M. Xu, *Nat. Commun.*, 2020, **11**, 1–9.
65 C. J. Zhang, M. P. Kremer, A. Seral-Ascaso, S. H. Park, N. McEvoy, B. Anasori, Y. Gogotsi and V. Nicolosi, *Adv. Funct. Mater.*, 2018, **28**, 1–10.
66 L. Yu, Z. Fan, Y. Shao, Z. Tian, J. Sun and Z. Liu, *Adv. Energy Mater.*, 2019, **9**, 1–8.
67 W. Yang, J. Yang, J. J. Byun, F. P. Moissinac, J. Xu, S. J. Haigh, M. Domingos, M. A. Bissett, R. A. Dryfe and S. Barg, *Adv. Mater.*, 2019, **31**, 1–8.